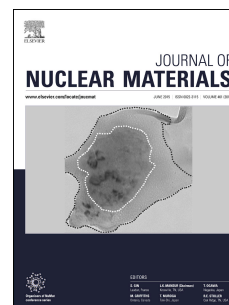


# Accepted Manuscript

Irradiation-induced amorphization in the zirconium suboxide on Zr-0.5Nb alloys

J. Liu, G. He, J. Hu, Z. Shen, M. Kirk, M. Li, E. Ryan, P. Baldo, S. Lozano-Perez, C. Grovenor



PII: S0022-3115(18)31193-0

DOI: <https://doi.org/10.1016/j.jnucmat.2018.11.015>

Reference: NUMA 51305

To appear in: *Journal of Nuclear Materials*

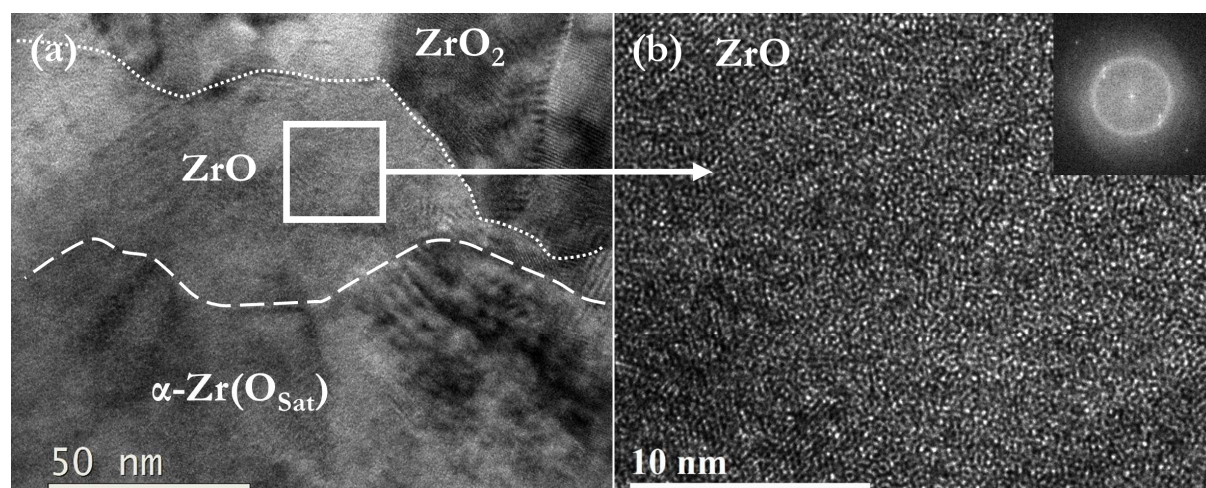
Received Date: 29 August 2018

Revised Date: 31 October 2018

Accepted Date: 12 November 2018

Please cite this article as: J. Liu, G. He, J. Hu, Z. Shen, M. Kirk, M. Li, E. Ryan, P. Baldo, S. Lozano-Perez, C. Grovenor, Irradiation-induced amorphization in the zirconium suboxide on Zr-0.5Nb alloys, *Journal of Nuclear Materials* (2018), doi: <https://doi.org/10.1016/j.jnucmat.2018.11.015>.

This is a PDF file of an unedited manuscript that has been accepted for publication. As a service to our customers we are providing this early version of the manuscript. The manuscript will undergo copyediting, typesetting, and review of the resulting proof before it is published in its final form. Please note that during the production process errors may be discovered which could affect the content, and all legal disclaimers that apply to the journal pertain.



Irradiation-induced amorphization in the zirconium suboxide on Zr-0.5Nb alloys

J. Liu<sup>1\*</sup>, G. He<sup>1</sup>, J. Hu<sup>2</sup>, Z. Shen<sup>1</sup>, M. Kirk<sup>2</sup>, M. Li<sup>2</sup>, E. Ryan<sup>2</sup>, P. Baldo<sup>2</sup>, S. Lozano-Perez<sup>1</sup>, C. Grovenor<sup>1</sup>

<sup>1</sup>Department of Materials, University of Oxford, Parks Road, OX1 3PH, United Kingdom

<sup>2</sup>Argonne National Laboratory, 9700 S. Cass Avenue, Argonne, IL 60439, United States

\*Corresponding author: [bryanchina@hotmail.com](mailto:bryanchina@hotmail.com)

## Abstract

We report for the first time the observation of irradiation-induced amorphization of the zirconium suboxide formed during aqueous corrosion of Zr-0.5Nb alloys. High-resolution transmission electron microscopy results reveal amorphization of the hexagonal-ZrO suboxide under heavy ion irradiation at cryogenic temperatures. This irradiation-induced amorphization behaviour is discussed in relation to the arrangement of oxygen interstitials and the formation of stable superlattices. The sensitivity of the suboxide to irradiation damage can lead to phase changes and the accumulation of defects near the oxide/metal interface, which needs to be taken into account in the development of mechanistic models addressing radiation-assisted acceleration of corrosion rates in zirconium alloys.

**Key words:** zirconium alloys, amorphous oxides, corrosion, irradiation, TEM

Zirconium alloys are universally used for fuel cladding and support structures in Pressurised Water Reactors (PWRs), but suffer from aqueous corrosion in service that can limit the operating lifetime and the effective burnup of the uranium fuel. Understanding the mechanisms of corrosion, especially under irradiation, is thus of great importance for undertaking more accurate, physically based lifetime predictions for cladding materials, and providing information to teams designing new corrosion-resistant alloys. Acceleration of the corrosion rate by up to factors of 6 has been reported as a result of exposure to in-reactor conditions [1-3], but the mechanisms of this accelerating effect are still not well understood. It has been correlated with the specific in-reactor coolant chemistry, intense  $\gamma$ -radiation or irradiation-induced redistribution of alloying elements in the oxide [4-7], but rather little attention has been paid to the influence of changes in the oxide phases under irradiation, especially at the oxide/metal interface. There has been recent discussion of the role of interfacial suboxide phases on the kinetics of oxidation [8-10], and a stoichiometric ZrO suboxide (h-ZrO) with a hexagonal structure and lattice parameters  $a = 5.31\text{\AA}$  and  $c = 3.20\text{\AA}$  has been both predicted theoretically and experimentally observed to form at the metal oxide interface in several fuel-cladding alloys at different stages of the corrosion process [11-16].

Previous work [17-19] on samples corroded in autoclaves has revealed that oxides formed on alloys with good corrosion performance generally have a well-aligned columnar oxide grain structure, fewer macro cracks, a thicker suboxide layer and a smoother oxide/metal ( $\text{ZrO}_2/\alpha\text{-Zr}$ ) interface, so all these microstructural features are potentially important in understanding the rate determining corrosion mechanisms. Recent corrosion tests using in-situ proton irradiation also showed accelerated corrosion kinetics [20] that matched the in-reactor kinetics at high burnups (after four cycles in PWRs [2]), and the oxide morphology formed in-reactor and under proton irradiation is similar, with a large volume fraction of cracks and fine pores present throughout the thickness of the oxide. With similar corrosion kinetics and damage rates (proton irradiation at  $4.4 \times 10^{-7} \text{dpa/s}$  versus neutron irradiation at  $2.8 \times 10^{-8}$  to  $7.8 \times 10^{-7} \text{dpa/s}$  [21, 22]), the oxide/metal interface region formed in-reactor and under ion irradiation corrosion is intended to experience similar cumulative damage levels and again have shown comparable grain morphologies in the oxide, an abundance of small, randomly oriented equiaxed grains [20, 23-25]. More recently, Garner et al [26] used scanning precession electron diffraction analysis in the transmission electron microscope and observed a more heterogeneous microstructure in reactor-formed oxides after 3 cycles, with reduced columnar grain growth compared with autoclave formed oxides. Moreover, proton irradiation up to 2dpa of an existing oxide layer did not show obvious changes in grain morphology [26], indicating the unique in-reactor equiaxed grain structure is not a direct result only of irradiation and as the authors suggested due to irradiation-induced modification of the nucleation and growth mechanisms of new oxide grains [24-26].

We have already shown that the combined thickness of the h-ZrO suboxide and the underlying layer of oxygen-saturated zirconium (with a stoichiometry close to  $\text{Zr}_3\text{O}$  and  $\alpha\text{-Zr}$  structure) at the metal/oxide interface correlates well to the instantaneous oxidation rate [5]. Whether the thickness of this interfacial layer is a cause or result of the observed slower corrosion rate, the presence of the ZrO suboxide and oxygen-saturated metal must contribute to controlling the rate of diffusion of the oxidising species to the metal matrix. The presence of suboxide between the Zr substrate and the growing bulk oxide at some

stages of the corrosion process may also play an important role in controlling the oxide microstructure described above by influencing the nucleation of new  $\text{ZrO}_2$  grains. Under irradiation, these nucleation and growth processes can be disrupted by high concentrations of defects generated at the oxide/metal interface [24-26]. In particular, any increase in local porosity [27, 28], and the resulting reduced cohesion between grains, may contribute to acceleration of the corrosion rate. Because of the key role that this region must play in determining the corrosion kinetics, it is also important to understand the processes by which the phases present at the metal/oxide interface may be damaged by irradiation.

Here we focus for the first time on direct experimental observation of irradiation-induced damage at this interface. The sample used in this study was prepared from a Westinghouse Zr-0.5Nb model alloy provided in tube format in the recrystallized condition. The sample was corroded in an autoclave filled with pure water at 360°C for 75 days to form an oxide of thickness  $\sim 2\mu\text{m}$ . Cross sectional transmission electron microscopy foils containing both the oxide layer and the metal matrix were prepared using the in-situ lift-out FIB method [29] on a Zeiss Crossbeam 540 FIB/SEM system with initial milling current of 7000-300pA at 30kV, and further thinned to a uniform thickness of  $\sim 50\text{ nm}$  using 2kV and 200pA. The distribution of the h-ZrO suboxide was precisely identified by the method given in [12] using Electron Energy Loss Spectroscopy (EELS). The EELS spectra were acquired on a JEOL ARM 200F TEM operated at 200kV with a step size of 4nm, a convergence angle of 30mrad and a collection angle of 40mrad. High-resolution transmission electron microscopy (HRTEM) observations were performed using a JEOL 3000F transmission electron microscope operating at 300kV. Fig. 1 shows typical pre-irradiation HRTEM images of crystalline phases at the oxide/metal interface. The fast Fourier transform (FFT) of the h-ZrO suboxide grain is indexed to be from a hexagonal crystal structure with zone axis close to  $[2\ \bar{1}\ \bar{1}\ 0]$ .

The specimen imaged in Fig. 1 was then irradiated in-situ in the Intermediate Voltage Electron Microscope (IVEM) at Argonne National Laboratory (ANL) using 1MeV  $\text{Kr}^{2+}$  ions up to a fluence of  $8.4 \times 10^{15}$  ions/ $\text{cm}^2$  at a rate of  $8 \times 10^{11}$  ions/ $\text{cm}^2/\text{s}$  on a cooling stage set at 50K. These conditions create damage very much faster than either neutron irradiation in a reactor environment or in the proton irradiation experiments described above, and were deliberately chosen to maximise the likelihood of identifying the phases most susceptible to radiation damage. The dpa rates for the bulk m- $\text{ZrO}_2$ , suboxide and metal matrix were calculated using SRIM [30] by selecting the Kinchin-Pease mode as recommended by Stoller [31], and are summarized in Table 1.

The h-ZrO suboxide is predicted to be a metastable phase of similar structure to the high-pressure  $\omega$ -Zr phase but with ordering of the interstitial oxygen [32, 33]. The oxygen content in the saturated solid solution in the metal matrix [ $\alpha$ -Zr( $\text{O}_{\text{Sat}}$ )] is  $\sim 30\text{ at.}\%$  [12] and oxygen is known to occupy the octahedral interstitial positions [34] while the volume of the Zr unit cell remains largely unchanged [32]. Displacement energies are set to 40eV and 28eV for Zr and O in h-ZrO suboxide,  $\alpha$ -Zr( $\text{O}_{\text{Sat}}$ ) and  $\alpha$ -Zr [35]. Higher displacement energies for Zr and O in m- $\text{ZrO}_2$  are required, and values of 120 eV for O and 80 eV for Zr [36] were used in our calculation. We note that the damage rate calculated by SRIM is mainly based on these chemical properties, so the influences of crystal structure, dose rate and temperature are not taken into consideration.

Table 1. Summary of properties of oxide, suboxide and Zr metal matrix, and damage rate calculated by SRIM for  $8 \times 10^{11}$  ions/ $\text{cm}^2/\text{s}$  1MeV  $\text{Kr}^{2+}$  ions

	Space group	Density ( $\text{g}/\text{cm}^3$ )	Defects/( $\text{\AA}$ -ion)	Damage rate (dpa/s)
m- $\text{ZrO}_2$	P2 <sub>1</sub> /c [37]	5.7	0.4	$3.7 \times 10^{-4}$
h-ZrO suboxide	P $\bar{6}$ 2m [32]	6.9	1.2	$1.2 \times 10^{-3}$
$\alpha$ -Zr( $\text{O}_{\text{Sat}}$ )	P6 <sub>3</sub> /mmc [32, 38]	6.8	1.1	$1.5 \times 10^{-3}$
$\alpha$ -Zr	P6 <sub>3</sub> /mmc [38]	6.5	1	$1.8 \times 10^{-3}$

Fig. 2(a and b) show in-situ observations of the oxide/metal interface, and in (d) an EELS O/Zr atomic ratio map of the initial sample in which we can identify the  $\text{ZrO}_2$  (bright white), Zr metal matrix (dark grey), and the intermediate contrast of h-ZrO grains and the oxygen-saturated metal ( $\alpha\text{-Zr}(\text{O}_{\text{sat}})$ ). The reverse contrast variations in the HAADF image in (c) are a result of changes in average atomic mass in the same phases. Based on (c) and (d), the location of suboxide grains can be identified precisely in (a) and (b), and lie between the dotted and dashed lines. The columnar m- $\text{ZrO}_2$  grains are clearly seen above h-ZrO suboxide grains  $\sim 30\text{nm}$  in diameter which separate the  $\alpha\text{-Zr}$  matrix and the bulk oxide along most of the metal/oxide interface.

Previous work has suggested that the loss of diffraction contrast in bright field TEM images is a useful indication of local amorphization [39]. Although we observed considerable changes in local contrast around the metal/oxide interface during the relatively early stages ( $10^{14}$  ions/ $\text{cm}^2$ ) of the in-situ experiment, no significant changes in contrast were observed in either the bulk oxide or metal matrix, Fig. 2(b). Interpreting these changes in contrast in-situ is complicated due to the unavoidable slight bending of the sample during irradiation which alters the diffraction conditions, so we carried out post-irradiation HRTEM analysis of oxide, suboxide and metal matrix regions, Fig. 3, after  $4 \times 10^{15}$  ions/ $\text{cm}^2$  (13dpa in h-ZrO). The complete amorphization of the h-ZrO grain was confirmed by HRTEM, Fig. 3(d). The oxygen saturated regions in the metal just beneath the h-ZrO suboxide layer showed some changes in contrast under irradiation, Fig. 3(b), but post-irradiation HRTEM characterization revealed that these oxygen saturated regions did not become fully amorphous, Fig. 3(c). More evidence showing the amorphization of the h-ZrO suboxide can be found in the supplementary data, Fig. S1. The post-irradiation samples were further characterized using EELS to determine the composition after ion irradiation, and the results in Fig. 4 indicate that the O content in the suboxide is, within experimental error, the same as before irradiation, so the heavy ion bombardment has not released the interstitial O to the microscope vacuum.

In these and similar experiments we have not observed amorphization of the m- $\text{ZrO}_2$  over a wide range of both temperature and damage levels up to a fluence of  $8.4 \times 10^{15}$  ions/ $\text{cm}^2$  (corresponding to 13dpa in h-ZrO and 19.1dpa in  $\alpha\text{-Zr}$ ). In the metal matrix, irradiation-induced dislocation loops have been widely studied [40] and have been well correlated with irradiation-induced hardening, swelling and elemental segregation [41-43]. In the current study, a high density of irradiation-induced c-loops can be seen in the metal matrix of the post-irradiation sample (see supplementary data, Fig. S2).

The exceptional irradiation resistance of the bulk oxide, compared with the suboxide and metal matrix, can in part be explained by the relatively low damage rate shown in Table 1. The characteristic oxide microstructure shown in Fig. 2 has a very fine grain size, 30-40 nm [10], and so contains a high density of grain boundaries that can act as strong sinks for radiation-induced point defects and limit the rate of damage accumulation [44]. In addition, it has been reported that oxygen vacancies in ionic lattices can enhance cation interstitial diffusion [45, 46], so that defects would have a higher likelihood of diffusing to these grain boundary sinks rather than accumulating locally.

By comparison, we observe much more severe radiation damage behaviour in the h-ZrO suboxide, and can propose mechanisms for this based on the previous literature [47-49] and our experimental observations. We observed the first signs of amorphization of the suboxide grains at a fluence of  $\sim 10^{14}$  ions/ $\text{cm}^2$ , corresponding to 0.16dpa in the h-ZrO. This behaviour is consistent with the homogeneous amorphization model of Motta and Olander [49, 50]. The basic postulate is that as the local concentration of point defects increases, a critical value is reached at which the lattice becomes unstable and collapses into an amorphous structure. In order to better understand the critical defect concentration at which amorphization occurs, a value of surviving defect fraction is required. Averback [51, 52] and Stoller [53] studied point defect production in Al, Cu and Fe at cryogenic temperatures ( $T \leq 100\text{K}$ ), and based on their results the value of surviving defect fraction can be estimated to be  $\sim 30\%$ . By applying this value to our experimental conditions, a critical defect concentration in the h-ZrO can be estimated to be 0.047 at a fluence of  $\sim 10^{14}$  ions/ $\text{cm}^2$  (0.16dpa), in good agreement with that proposed by Swanson [54] who



reported a defect concentration between 0.02 and 0.04 is required for collapse of the lattice into an amorphous state.

The local defect concentrations, particularly in the h-ZrO grains that became fully amorphous, will be a result of several competing factors. We have estimated that the damage rate in the suboxide is as high as 0.0012dpa/s, Table 1. The oxygen atoms in the interstitial positions are displaced more easily than Zr so an ordered interstitial arrangement of O atoms is damaged particularly fast, resulting in a high local defect concentration [48]. However, irradiation-induced thermal spikes will induce thermal recombination and lead to the annihilation of point defects. Free surfaces and grain boundaries can also serve as strong sinks for point defects, although the rate of both defect migration and annihilation processes will be reduced to some extent by the choice of 50K for the sample temperature during irradiation. While the damage rate in the metal matrix is also very high, no amorphization was observed, presumably as a result of the efficient incorporation of point defects into dislocation loops at relatively low defect concentrations,  $\sim 10^{-4}$  [55], although it has been reported that oxygen in solid solution in Zr can suppress the diffusion of point defects [56, 57].

Thermodynamic modelling shows that the h-ZrO suboxide phase, which is absent in the traditional Zr-O binary phase diagram [58], is actually an equilibrium phase over a very narrow oxygen partial pressure window [32]. Ab-initio studies predict this h-ZrO to have a structure similar to the high-pressure  $\omega$ -Zr phase, but with the oxygen in an ordered arrangement [11, 32]. Assuming that this ordered interstitial structure plays a role in stabilizing the metastable h-ZrO [11], we can explain the observed amorphization behavior as destruction of the ordering in the preformed h-ZrO grains in the TEM sample by ion-irradiation to the high dpa levels used here. This same model can also be applied to explain the irradiation-induced amorphization of some other intermetallic compounds in zirconium alloys. For example, it has been widely reported that crystalline-amorphous transformations occur in intermetallic precipitates such as  $\text{Zr}(\text{Nb},\text{Fe})_2$ ,  $\text{Zr}_2(\text{Fe}, \text{Ni})$  and  $\text{Zr}(\text{Cr},\text{Fe})_2$  under electron, ion and neutron irradiation over a large temperature range [49, 50, 59-61]. These Fe-enriched precipitates are known to have interstitial iron ordering to form superlattice structures [59, 62, 63], which may then be easily amorphized under irradiation. On the other hand, irradiation-induced amorphization has never been reported in  $\beta$ -Nb precipitates which do not have an ordered interstitial structure.

Under reactor conditions, the ongoing corrosion process means that suboxide grains are constantly reformed as the oxide layer thickens, such that the damage accumulated in each h-ZrO grain is limited. Using the kinetic data in [5] to estimate the rate at which h-ZrO grains are formed and consumed at the metal-oxide interface and a damage rate of  $10^{-7}$  dpa/s [21, 22], the maximum damage accumulated in any individual suboxide grain can be estimated to be around 0.1 dpa. Thus although amorphisation of the suboxide is unlikely to occur under reactor conditions, in agreement with the observation of crystalline h-ZrO layers in both neutron- and ion-irradiated samples in the literature [10, 26], we have observed that the h-ZrO is more susceptible to radiation damage than the surrounding phases. Although more study is needed to address the evolution in-reactor of the microstructure and defect content of this interface suboxide region, and its impact on the corrosion kinetics, some specific aspects to focus on can be suggested from consideration of previously reported irradiation effects in other materials. At the in-reactor temperature,  $\sim 270$ - $360^\circ\text{C}$ , the higher mobility of radiation-induced defects can result in the nucleation and growth of defects clusters, e.g. dislocation loops and voids, in the hexagonal suboxide, and especially the voids can have a strong effect on local transport of oxidizing species. Other effects such as irradiation-induced growth and swelling may also occur preferentially in the interfacial suboxide phase, and the related strain and density changes can effect phase transformations as the underlying metal oxidized to bulk  $\text{ZrO}_2$ . All these effects can modify local diffusion rates, the nucleation and growth process of new h-ZrO and  $\text{ZrO}_2$  grains, and give rise to increased porosity, and so be a potent mechanism for radiation-assisted acceleration of the overall corrosion rate [24-26].

In a summary, we report in-situ observations at high damage rates of irradiation-induced amorphization of the thin layer of h-ZrO suboxide formed during aqueous corrosion of Zr alloys. A possible

explanation for the enhanced damage susceptibility of the suboxide phase has been proposed to be the destruction of the ordered arrangement of oxygen interstitials that stabilises this metastable phase. We suggest that this sensitivity of the suboxide to irradiation damage needs to be incorporated into mechanistic models for the corrosion behaviour of zirconium alloys even at lower damage rates.

## Acknowledgements

The authors acknowledge the contribution made to this work by their collaborators from Westinghouse and the MUZIC-2 project providing zirconium samples. EPSRC grants (EP/K040375/1 and EP/N010868/1) are acknowledged for funding the 'South of England Analytical Electron Microscope' and the Zeiss Crossbeam FIB/SEM used in this research. We would also like to thank Dr. Rebecca Nicholls for helpful discussions.

## References

- [1] E. Hillner, D.G. Franklin, J.D. Smee, *Journal of Nuclear Materials*, 278 (2000) 334-345.
- [2] V. Bouineau, G. Bénier, D. Pêcheur, J. Thomazet, A. Ambard, M. Blat, *Nuclear Technology*, 170 (2010) 444-459.
- [3] G. Garner, B. Hilton, E. Mader, *Proceedings of the 2007 LWR Fuel Performance Meeting/TopFuel 2007'Zero by 2010', 2007.*
- [4] T. Kido, K. Kanasugi, M. Sugano, K. Komatsu, *Journal of Nuclear Materials*, 248 (1997) 281-287.
- [5] B. Cox, *Journal of Nuclear Materials*, 336 (2005) 331-368.
- [6] B. Zhou, Q. Li, M. Yao, W. Liu, Y. Chu, *Zirconium in the Nuclear Industry: 15th International Symposium*, ASTM International, 2009, pp. 360-383.
- [7] D. Rishel, B. Kammenzind, *Zirconium in the Nuclear Industry: 18th International Symposium*, ASTM International, 2018, pp. 555-595.
- [8] M. Preuss, P. Frankel, S. Lozano-Perez, D. Hudson, E. Polatidis, N. Ni, J. Wei, C. English, S. Storer, K. Chong, M. Fitzpatrick, P. Wang, J. Smith, C. Grovenor, G. Smith, J. Sykes, B. Cottis, S. Lyon, L. Hallstadius, B. Comstock, A. Ambard, M. Blat-Yrieix, *Zirconium in the Nuclear Industry: 16th International Symposium*, ASTM International, 2011, pp. 649-681.
- [9] Y. Dong, A.T. Motta, E.A. Marquis, *Journal of Nuclear Materials*, 442 (2013) 270-281.
- [10] J. Hu, B. Setiadinata, T. Aarholt, A. Garner, A. Vilalta-Clemente, J. Partezana, P. Frankel, P. Bagot, S. Lozano-Perez, A. Wilkinson, M. Preuss, M. Moody, C.R.M. Grovenor, *Zirconium in the Industry: 18th International Symposium*, ASTM International, 2018, pp. 93-126.
- [11] R.J. Nicholls, N. Ni, S. Lozano-Perez, A. London, D.W. McComb, P.D. Nellist, C.R.M. Grovenor, C.J. Pickard, J.R. Yates, *Advanced Engineering Materials*, 17 (2015) 211-215.
- [12] J. Hu, A. Garner, N. Ni, A. Gholinia, R.J. Nicholls, S. Lozano-Perez, P. Frankel, M. Preuss, C.R.M. Grovenor, *Micron*, 69 (2015) 35-42.
- [13] A. Yilmazbayhan, E. Breval, A.T. Motta, R.J. Comstock, *Journal of Nuclear Materials*, 349 (2006) 265-281.
- [14] N. Ni, S. Lozano-Perez, J. Sykes, C. Grovenor, *Ultramicroscopy*, 111 (2011) 123-130.
- [15] H. Yu, Z. Yao, F. Long, P. Saidi, M.R. Daymond, *Journal of Applied Crystallography*, 50 (2017) 1028-1035.
- [16] K.J. Annand, I. MacLaren, M. Gass, *Journal of Nuclear Materials*, 465 (2015) 390-399.
- [17] A. Yilmazbayhan, A.T. Motta, R.J. Comstock, G.P. Sabol, B. Lai, Z. Cai, *Journal of Nuclear Materials*, 324 (2004) 6-22.
- [18] A. Garner, A. Gholinia, P. Frankel, M. Gass, I. MacLaren, M. Preuss, *Acta Materialia*, 80 (2014) 159-171.
- [19] H. Beie, A. Mitwalsky, F. Garzarolli, H. Ruhmann, H. Sell, *Zirconium in the nuclear industry: 10th international symposium*, ASTM International, 1994, pp. 615-643.
- [20] P. Wang, G.S. Was, *Journal of Materials Research*, 30 (2015) 1335-1348.
- [21] V. Shishov, M. Peregud, A. Nikulina, Y.V. Pimenov, G. Kobylansky, A. Novoselov, Z. Ostrovsky, A. Obukhov, *Zirconium in the Nuclear Industry: 14th International Symposium*, ASTM International, 2005, pp. 666-686.



- [22] A.Y. Rogozyanov, A. Smirnov, B. Kanashov, V. Polenok, A. Nuzhdov, Zirconium in the Nuclear Industry: 14th International Symposium, ASTM International, 2005, pp. 651-665.
- [23] X. Iltis, F. Lefebvre, C. Lemaignan, *Journal of Nuclear Materials*, 224 (1995) 109-120.
- [24] X. Iltis, F. Lefebvre, C. Lemaignan, Zirconium in the Nuclear Industry: 11th International Symposium, ASTM International, 1996, pp. 242-264.
- [25] S. Abolhassani, R. Restani, T. Rebac, F. Groeschel, W. Hoffelner, G. Bart, W. Goll, F. Aeschbach, Zirconium in the Nuclear Industry: 14th International Symposium, ASTM International, 2005, pp. 467-493.
- [26] A. Garner, F. Baxter, P. Frankel, M. Topping, A. Harte, T. Slater, P. Tejlund, J. Romero, E. C Darby, A. Cole-Baker, M. Gass, M. Preuss, Zirconium in the Nuclear Industry: 18th International Symposium, ASTM International, 2018, pp. 491-523.
- [27] N. Ni, S. Lozano-Perez, M.L. Jenkins, C. English, G.D.W. Smith, J.M. Sykes, C.R.M. Grovenor, *Scripta Materialia*, 62 (2010) 564-567.
- [28] N. Ni, S. Lozano-Perez, J.M. Sykes, G.D.W. Smith, C.R.M. Grovenor, *Corrosion Science*, 53 (2011) 4073-4083.
- [29] S. Lozano-Perez, *Micron*, 39 (2008) 320-328.
- [30] J.F. Ziegler, M.D. Ziegler, J.P. Biersack, *Nuclear Instruments and Methods in Physics Research Section B: Beam Interactions with Materials and Atoms*, 268 (2010) 1818-1823.
- [31] R.E. Stoller, M.B. Toloczko, G.S. Was, A.G. Certain, S. Dwaraknath, F.A. Garner, *Nuclear Instruments and Methods in Physics Research Section B: Beam Interactions with Materials and Atoms*, 310 (2013) 75-80.
- [32] B. Puchala, A. Van der Ven, *Physical Review B*, 88 (2013) 094108.
- [33] P. Bossis, G. Lelievre, P. Barberis, X. Iltis, F. Lefebvre, Zirconium in the Nuclear Industry: 12th International Symposium, ASTM International, 2000, pp. 918-927.
- [34] M. Hirabayashi, S. Yamaguchi, T. Arai, H. Asano, S. Hashimoto, *Physica Status Solidi (a)*, 23 (1974) 331-339.
- [35] ASTM E521, *Annu. B. ASTM Stand.*, ASTM, West Conshohocken, PA, 2009
- [36] J. M. Costantini, F. Beuneu, *physica status solidi (c)*, 4 (2007) 1258-1263.
- [37] J.D. McCullough, K.N. Trueblood, *Acta Crystallographica*, 12 (1959) 507-511.
- [38] A.W. Hull, *Physical Review*, 18 (1921) 88-89.
- [39] B. Fultz, J. Howe, *Diffraction Contrast in TEM Images, Transmission Electron Microscopy and Diffractometry of Materials*, Springer Berlin Heidelberg, Berlin, Heidelberg, 2013, pp. 349-427.
- [40] A. Jostsons, P.M. Kelly, R.G. Blake, *Journal of Nuclear Materials*, 66 (1977) 236-256.
- [41] S.I. Choi, J.H. Kim, *Nuclear Engineering and Technology*, 45 (2013) 385-392.
- [42] M. Topping, A. Harte, P. Frankel, G. Sundell, M. Thuvander, H.O. Andren, D. Jadernas, P. Tejlund, J. Romero, E.C. Darby, S. Dumbill, L. Hallstadius, M. Preuss, The Effect of Iron on Dislocation Evolution in Model and Commercial Zirconium Alloys, Zirconium in the Nuclear Industry: 18th Symposium, ASTM International, 2018, pp. 796-822.
- [43] A. Harte, D. Jädernas, M. Topping, P. Frankel, C.P. Race, J. Romero, L. Hallstadius, E.C. Darby, M. Preuss, *Acta Materialia*, 130 (2017) 69-82.
- [44] B.P. Uberuaga, L.J. Vernon, E. Martinez, A.F. Voter, *Scientific Reports*, 5 (2015) 9095.
- [45] D.S. Aidhy, Y. Zhang, W.J. Weber, *Scripta Materialia*, 98 (2015) 16-19.
- [46] R.C. Ewing, W.J. Weber, J. Lian, *Journal of Applied Physics*, 95 (2004) 5949-5971.
- [47] W.J. Weber, *Nuclear Instruments and Methods in Physics Research Section B: Beam Interactions with Materials and Atoms*, 166-167 (2000) 98-106.
- [48] D.A. Thompson, *Radiation Effects*, 56 (1981) 105-150.
- [49] A.T. Motta, D.R. Olander, *Acta Metallurgica et Materialia*, 38 (1990) 2175-2185.
- [50] A.T. Motta, L.M. Howe, P.R. Okamoto, *Journal of Nuclear Materials*, 205 (1993) 258-266.
- [51] R.S. Averback, R. Benedek, K.L. Merkle, J. Sprinkle, L.J. Thompson, *Journal of Nuclear Materials*, 113 (1983) 211-218.
- [52] R.S. Averback, *Journal of Nuclear Materials*, 108-109 (1982) 33-45.
- [53] R.E. Stoller, G.R. Odette, B.D. Wirth, *Journal of Nuclear Materials*, 251 (1997) 49-60.
- [54] M.L. Swanson, J.R. Parsons, C.W. Hoelke, *Radiation Effects*, 9 (1971) 249-256.
- [55] J.L. Brimhall, E.P. Simonen, H.E. Kissinger, *Journal of Nuclear Materials*, 48 (1973) 339-350.
- [56] M. Griffiths, D. Gilbon, C. Regnard, C. Lemaignan, *Journal of Nuclear Materials*, 205 (1993) 273-283.
- [57] C. Hellio, C.H. de Novion, L. Boulanger, *Journal of Nuclear Materials*, 159 (1988) 368-378.

- [58] J. Abriata, J. Garces, R. Versaci, *Bulletin of Alloy Phase Diagrams*, 7 (1986) 116-124.
- [59] A.T. Motta, C. Lemaignan, *Journal of Nuclear Materials*, 195 (1992) 277-285.
- [60] S. Valizadeh, G. Ledergerber, S. Abolhassan, D. Jädernäs, M. Dahlbäck, E. Mader, G. Zhou, J. Wright, and L. Hallstadius, *Zirconium in the Nuclear Industry: 16th International Symposium*. ASTM International, 2011, pp. 729-753.
- [61] A.T. Motta, F. Lefebvre, C. Lemaignan, *Zirconium in the Nuclear Industry: 9th International Symposium*, ASTM International, 1991, pp. 718-722.
- [62] P. Burr, S. Murphy, S. Lumley, M. Wenman, R. Grimes, *Corrosion Science*, 69 (2013) 1-4.
- [63] P. Burr, M. Wenman, B. Gault, M. Moody, M. Ivermark, M. Rushton, M. Preuss, L. Edwards, R. Grimes, *Journal of Nuclear Materials*, 467 (2015) 320-331.

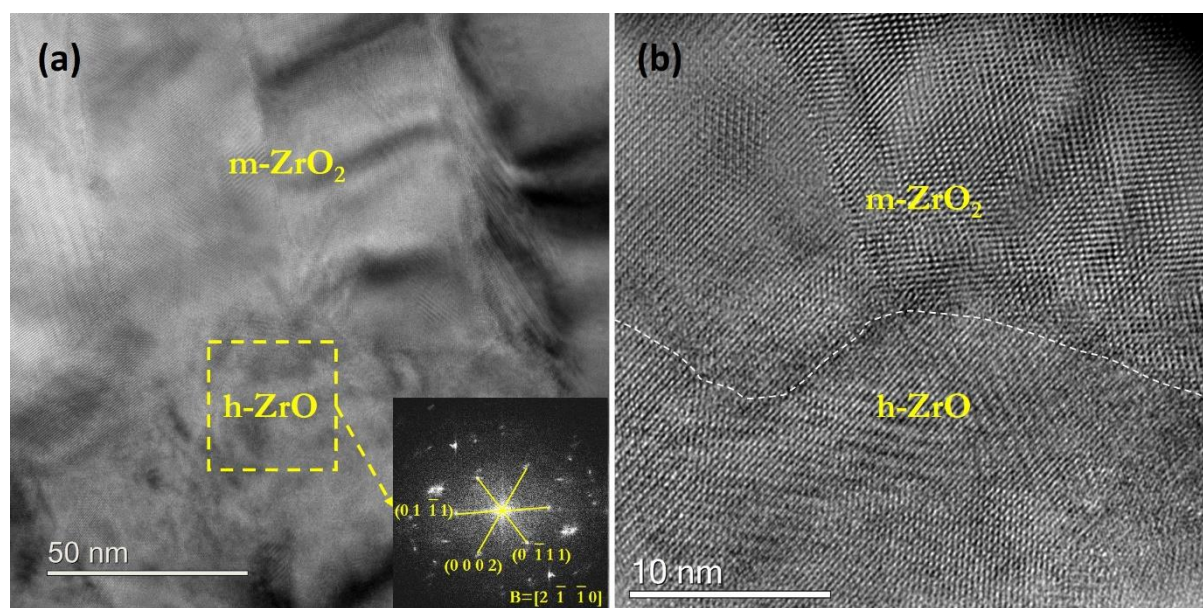


Fig. 1. Pre-irradiation HRTEM images of a typical region of oxide/metal interface identifying the columnar monoclinic  $\text{ZrO}_2$  (m- $\text{ZrO}_2$ ) grains. (a) low-magnification with FFT from an h- $\text{ZrO}$  suboxide grain. (b) high-magnification image showing the atomic structure in m- $\text{ZrO}_2$  and h- $\text{ZrO}$ .

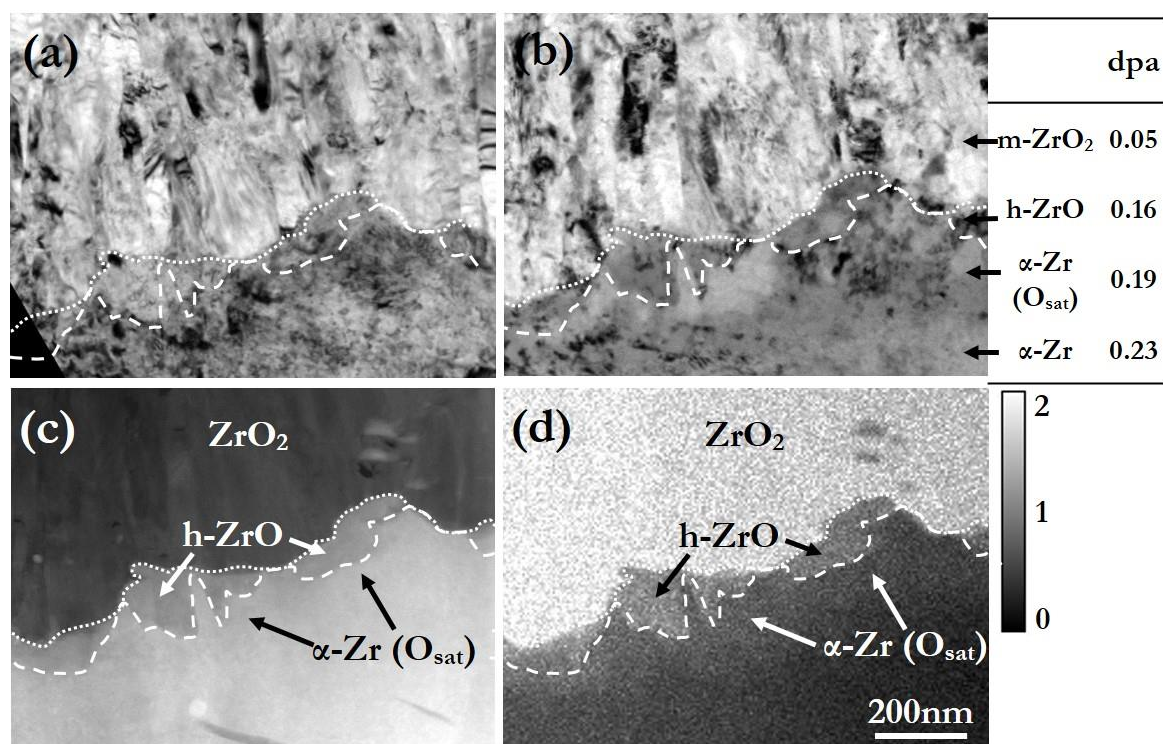


Fig. 2. (a, b) In-situ TEM images showing the microstructure of oxide, suboxide and metal substrate in the Zr-0.5Nb alloy at different damage levels: (a) pre-irradiation (b)  $10^{14}$  ions/cm<sup>2</sup>, the corresponding damage levels in dpa are also shown on the right, (c) pre-irradiation HAADF STEM image of the region followed during in-situ irradiation and (d) O/Zr atomic ratio map from EELS analysis of the pre-irradiation sample. The dotted lines indicate the oxide/suboxide interface, and the dashed lines the suboxide/metal interface.



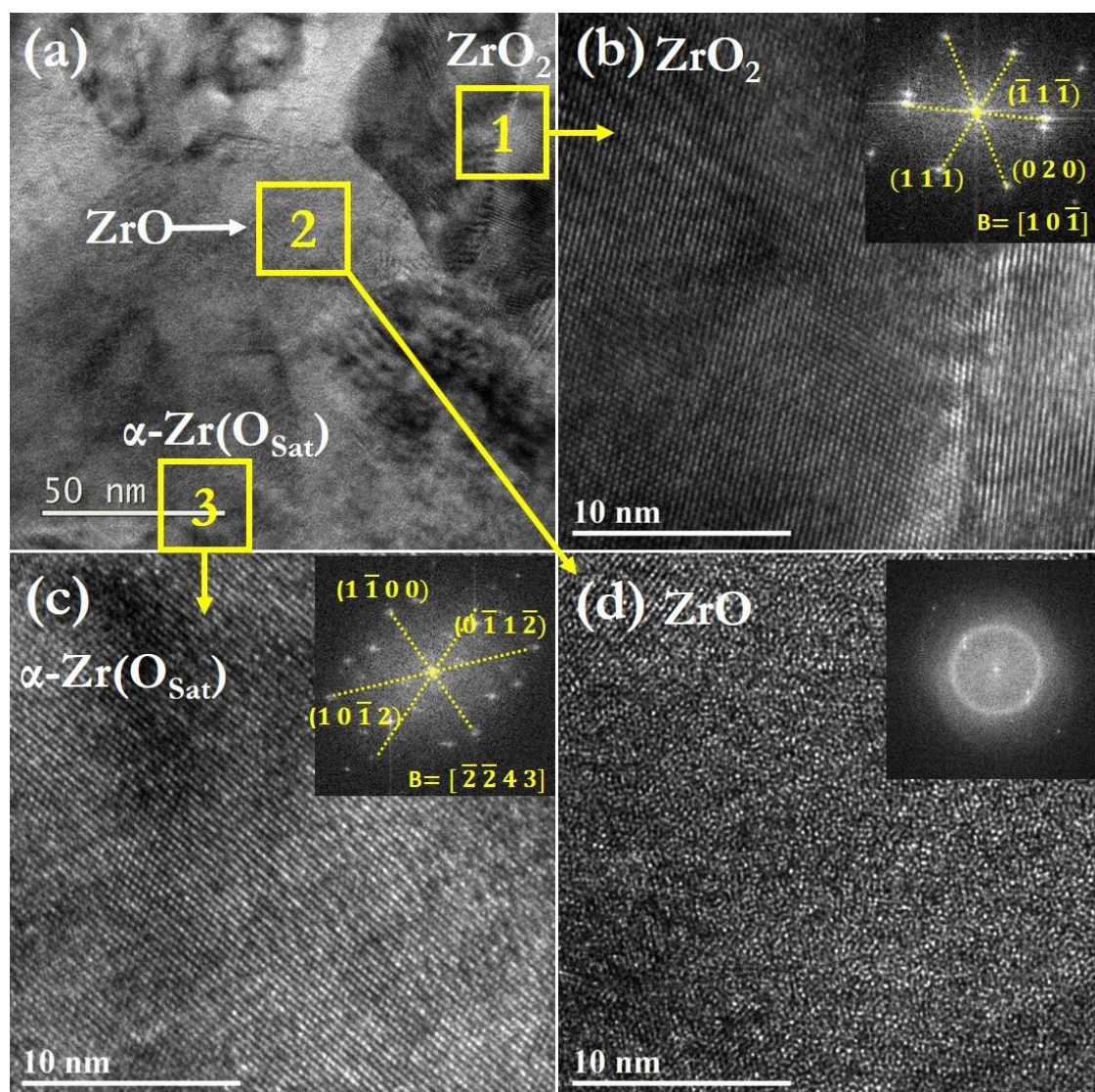


Fig. 3. (a) low magnification bright field TEM image showing the m- $\text{ZrO}_2$ , h- $\text{ZrO}$  suboxide and  $\alpha\text{-Zr}(\text{O}_{\text{Sat}})$  after irradiation to  $8.4 \times 10^{15}$  ions/ $\text{cm}^2$  (13dpa in h- $\text{ZrO}$  and 19.1dpa in  $\alpha\text{-Zr}$ ). (b) HRTEM and FFT from the region of m- $\text{ZrO}_2$  identified in (a). (c and d) HRTEM and FFT from the identified regions of  $\alpha\text{-Zr}(\text{O}_{\text{Sat}})$  and h- $\text{ZrO}$  suboxide respectively.



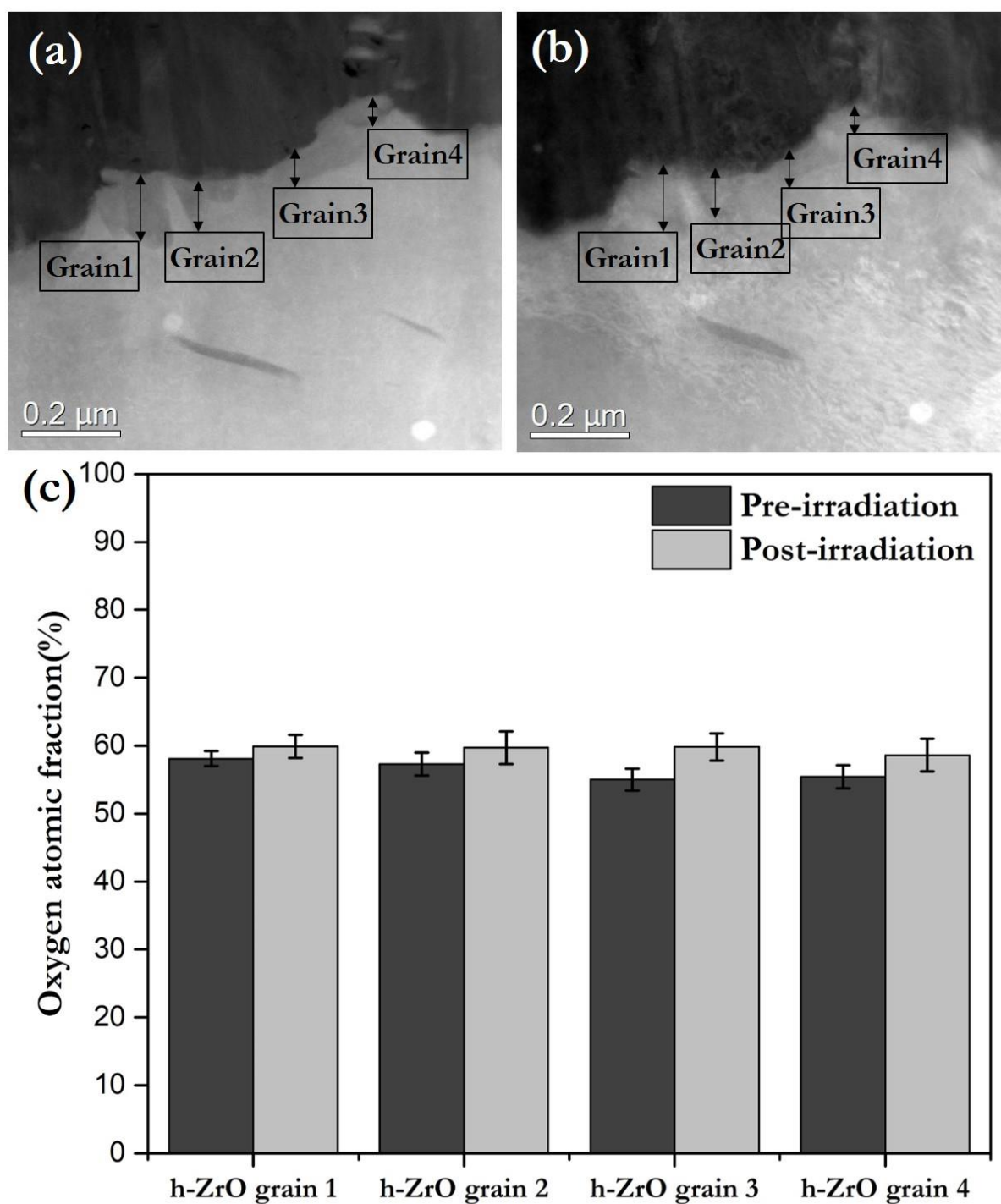


Fig. 4. HAADF STEM images from the same area of (a) pre-irradiation and (b) post-irradiation samples. (c) Comparison of oxygen concentrations in the suboxide grains pre- and post-irradiation calculated from EELS spectra acquired from the regions highlighted in (a) and (b). The oxygen concentrations were calibrated by assuming the value in the bulk  $\text{ZrO}_2$  far from the interface to be 66%.